A search for radius inflation among active M-dwarfs in Praesepe

R. J. Jackson[1], R. D. Jeffries[1], Constantine P. Deliyannis[2], Qinghui Sun[2]
and Stephanie. T. Douglas[3,4]

[1] *Astrophysics Group, Keele University, Keele, Staffordshire ST5 5BG*
[2] *Department of Astronomy, Indiana University. 727 E 3rd Street, Bloomington, IN 47405-7105, USA*
[3] *Harvard-Smithsonian Center for Astrophysics, 60 Garden Street, Mailstop 15, Cambridge, MA, USA*
[4] *NSF Astronomy & Astrophysics Postdoctoral Fellow*

ABSTRACT

Rotation periods from Kepler K2 are combined with projected rotation velocities from the WIYN 3.5-m telescope, to determine projected radii for fast-rotating, low-mass ($0.15 \leqslant M/M_\odot \leqslant 0.6$) members of the Praesepe cluster. A maximum likelihood analysis that accounts for observational uncertainties, binarity and censored data, yields marginal evidence for radius inflation – the average radius of these stars is 6 ± 4 per cent larger at a given luminosity than predicted by commonly-used evolutionary models. This over-radius is smaller (at 2-sigma confidence) than was found for similar stars in the younger Pleiades using a similar analysis; any decline appears due to changes occurring in higher mass ($> 0.25 M_\odot$) stars. Models incorporating magnetic inhibition of convection predict an over-radius, but do not reproduce this mass dependence unless super-equipartition surface magnetic fields are present at lower masses. Models incorporating flux-blocking by starspots can explain the mass dependence but there is no evidence that spot coverage diminishes between the Pleiades and Praesepe samples to accompany the decline in over-radius. The fastest rotating stars in both Praesepe and the Pleiades are significantly smaller than the slowest rotators for which a projected radius can be measured. This may be a selection effect caused by more efficient angular momentum loss in larger stars leading to their progressive exclusion from the analysed samples. Our analyses assume random spin-axis orientations; any alignment in Praesepe, as suggested by Kovacs (2018), is strongly disfavoured by the broad distribution of projected radii.

Key words: stars: magnetic activity; stars: low-mass – stars: evolution – stars: pre-main-sequence – clusters and associations: general – starspots

1 INTRODUCTION

There are significant differences between the predictions of stellar models and the precisely measured masses and radii of main-sequence K- and M-dwarfs in eclipsing binary systems. For a given mass, the absolute radii of some stars with $0.2 < M/M_\odot < 0.8$ are 10–20 per cent larger than predicted and hence, for a given luminosity, the effective temperature, $T_{\rm eff}$ may be under-estimated by 5–10 per cent (e.g. Lopez-Morales & Ribas 2005; Morales et al. 2009; Torres 2013). Since the interferometrically determined radii of nearby, slowly rotating low-mass stars are in better agreement with "standard" evolutionary models, it has been hypothesised that the enlarged radii of fast-rotating binary components, are due to dynamo-generated magnetic activity; either through inhibiting convection (e.g. Mullan & MacDonald 2001; Feiden & Chaboyer 2014) or by blocking outward flux with dark starspots (e.g. Spruit & Weiss 1986; MacDonald & Mullan 2013; Jackson & Jeffries 2014a).

There is growing indirect evidence that this phenomenon also occurs in fast-rotating young pre main sequence (PMS) and zero-age main sequence (ZAMS) stars and may play a role in the explanation of several astrophysical problems affecting stars with deep convective envelopes, rapid rotation and high levels of magnetic activity. These include the anomalously red colours of PMS/ZAMS stars; the rotation-dependent scatter in lithium depletion seen in young stars of otherwise similar mass and age; and disagreements between measured mass, radius and position in the Hertzsprung-Russell (HR) diagram for several PMS/ZAMS eclipsing binaries (see for example Somers & Pinsonneault 2014; Jackson & Jeffries 2014a; Covey et al. 2016; Feiden 2016; Kraus et al. 2016, 2017; Jeffries et al. 2017; Somers & Stassun 2017; Bouvier et al. 2018).

Direct determination of the radii of young stars by interferometric techniques is hampered by their distance. An indirect approach measures the projected radii of stars by combining the rotation period (P in days) with the projected equatorial velocity

($v \sin i$ in km s^{-1}):

$$\frac{R \sin i}{R_\odot} = 0.0198 \, P \, v \sin i \tag{1}$$

(e.g. Rhode, Herbst & Mathieu 2001; Jeffries 2007). If the spin axis orientation of the stars is random (e.g. Jackson & Jeffries 2010) and observational biases are understood, then a set of $R \sin i$ estimates can be modelled to determine the true average radius for a group of stars. This technique has been used to claim the detection of inflated radii in the young K- and M-type stars of several young clusters, notably the Pleiades at an age of $\simeq$ 120 Myr (Jackson, Jeffries & Maxted 2009; Hartman et al. 2010; Jackson & Jeffries 2014a; Jackson et al. 2016; Lanzafame et al. 2017).

In Jackson et al. (2018, hereafter Paper I), we obtained the largest ever set of homogeneously determined values of $v \sin i$ and P for low-mass stars in the Pleiades to investigate radius inflation as a function of mass using Eqn. 1. It was established that stars with $0.1 < M/M_\odot < 0.8$ are 14 ± 2 per cent larger than predicted by standard evolutionary models (e.g. Dotter et al. 2008; Baraffe et al. 2015) at a given luminosity, with no evidence for a strong mass-dependence. The lack of mass-dependence is incompatible with published evolutionary models that incorporate the inhibition of convection by magnetic fields (e.g. Feiden, Jones & Chaboyer 2015), but might be consistent with a mass-dependent starspot coverage or some combination of the two effects.

A critical diagnostic would be to see whether radius inflation is only associated with the rapid rotation of these low-mass stars, or whether their age and hence evolutionary stage and interior structure are important. A very similar analysis of a heterogeneous (but presumably much older than the Pleiades) sample of fast-rotating field M-dwarfs also found inflation levels of 14 ± 3 per cent compared with non-magnetic evolutionary models, suggesting that age itself may not be a vital parameter (Kesseli et al. 2018). In this paper, we extend the work of Paper I to a homogeneous population of coeval, fast-rotating low-mass stars in the older ($\simeq$ 650 Myr) Praesepe cluster, with measured rotation periods from the Kepler K2 mission and new measurements of $v \sin i$ using the WIYN-3.5m telescope and Hydra spectrograph. Whilst M-dwarfs in the Pleiades are still in the PMS phase (or have just reached the ZAMS), stars of equivalent mass in Praesepe should be firmly established on the hydrogen-burning main sequence and those with mass $M \geqslant 0.35 M_\odot$ should have radiative cores (Baraffe et al. 2015).

2   SPECTROSCOPIC OBSERVATIONS

2.1   Target selection

Candidate targets were selected from a list of high probability Praesepe members (from Kraus & Hillenbrand 2007) with rotation periods reported by Douglas et al. (2017). The large majority of these periods (92 per cent) are based on K2 light curves from campaign 5 (Howell et al. 2014) and the completeness of the rotation period data is 86 per cent. Stars with rotation periods were matched with the 2MASS catalogue (Skrutskie el al. 2006) to define the target names, co-ordinates and K_{2MASS}, and with the Gaia catalogue (DR1, Gaia collaboration 2016) for G magnitudes. Figure 1a shows the spatial distribution of potential targets. Targets for our fibre-spectroscopy were selected from a 10 square degree area with the highest target density, with a faint limit of $K_{2MASS} < 14.5$.

The luminosity of each target was estimated from its K_{CIT} magnitude (hereafter referred to as K) assuming a conversion of

$K = K_{2MASS} + 0.024$ (Carpenter 2001), zero reddening (Cummings et al. 2017), a distance modulus of 6.35±0.04 (Gaia Collaboration et al. 2018) , and taking bolometric corrections as a function of $(V - K)_0$ from a 625 Myr Baraffe et al. (2015; hereafter BHAC15) isochrone. V magnitudes were only available for 54 per cent of the stars. This subset was used to define a second-order polynomial relationship between $V - K$ and $G - K$ (shown in Fig. 2) that allows the assignment of $V - K$, bolometric corrections and luminosities to the other stars, with an rms uncertainty of ± 0.17 mag in $V - K$, corresponding to ± 0.07 dex in log luminosity. The colour-magnitude diagram for potential targets is shown in Fig.1b.

Targets were prioritised according to a predicted projected equatorial velocity, $(v \sin i)_p = 50 \, (\pi/4) \, R/P$ in km s^{-1}, where R is the stellar radius in solar units estimated from the 625 Myr BHAC15 isochrone and $\pi/4$ is a simple average value for the (unknown) $\sin i$ if the spin axes are randomly oriented. Targets with $(v \sin i)_p > 8$ km s^{-1} were given the highest weighting for target selection, since these were likely to yield a resolvable $v \sin i$ (see Fig 1c). The BHAC15 models are calculated at a solar metallicity, but Praesepe has a super-solar metallicity ([Fe/H]=0.156±0.004 – Cummings et al. 2017). The effect of metallicity on the estimated over-radius is considered in section 4.

2.2   Observations

Observations of the Praesepe targets were made in a similar manner to that described in Paper I at the WIYN 3.5-m telescope using the WIYN Hydra multi-object spectrograph (Bershady et al. 2008). Eleven configurations were observed in Praesepe over the period from 3 January 2017 to 22 February 2017. Field centres were chosen to maximise the number of highest priority targets. The first 7 configurations were observed using the "blue" Hydra fibres giving a resolving power of 14000 (determined from the line width of the arc spectra). These observations were made on the same nights and with the same telescope set up as previously reported observations of Pleiades targets (Paper I). The final 4 configurations were observed using the "red" Hydra fibres giving an increased resolving power of 19000. Spectra were recorded over a $\sim$ 400Å interval, centred at $\sim$ 7880Å. The FWHM of a resolution element was sampled by about 2.5 (binned) pixels. Details of the configuration and exposure times are given in Table 1. Long exposures were split into multiples of about 1 hour to aid cosmic ray rejection. A total of 446 spectra were measured for 230 unique targets in Praesepe, 283 using blue Hydra fibres and 163 using the red fibres. Properties of the observed targets are listed in Table 2.

2.3   Data reduction

Many targets were faint, requiring optimal extraction of their spectra to provide sufficient signal-to-noise ratio (SNR) for useful analysis. Strong sky emission lines dominated the fainter spectra. For these reasons we used purpose-built software for data reduction, described in detail in Paper I, but summarised here. De-biased science data images were normalised to daytime tungsten lamp flat field exposures. Spectra were extracted from the normalised image using an optimal extraction algorithm (Horne 1986). Daytime Th-Ar lamp exposures were used to define polynomial relations between pixels in the extracted spectra and wavelength, and a correction applied to the target exposures based on the position of prominent sky emission lines in the median blank sky spectra. The spectra
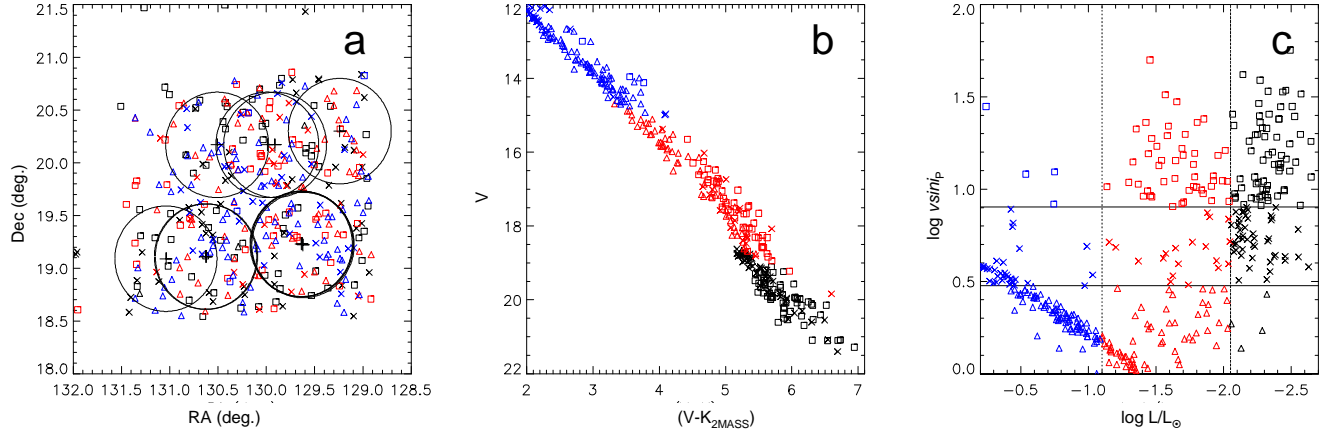
Figure 1. Target selection: Panel (a) shows the spatial distribution of targets. Circles show the field of view of the eleven observed WIYN Hydra configurations (see Table 1). The different symbols correspond to divisions in estimated luminosity shown in panels (b) and (c), and the different symbol shapes correspond to the predicted observed $(v \sin i)_p$ (see section 2.1) shown in panel (c) – triangles indicate $(v \sin i)_p < 3 \mathrm{km\,s^{-1}}$, crosses have $3 < (v \sin i)_p < 8 \mathrm{\,km\,s^{-1}}$ and squares $(v \sin i)_p \geqslant 8 \mathrm{\,km\,s^{-1}}$. Panel (b) shows V versus $V - K_{2\mathrm{MASS}}$ colour magnitude diagram for the same data set using the same symbols and colour coding. Panel (c) shows $(v \sin i)_p$ as a function of estimated target luminosity.

Table 1. Hydra Configurations observed in Praesepe. The positions are those of the field centres.

| Config. number	File number	Hydra fibres	Date	UT of exposure #1	RA (J2000)	Dec	Number exposures	Total Exp. time (s)	Fibres on targets	Fibres on sky
1	4058	blue	2017-01-03	10:16:59.0	+08:39:37.70	+20:09:58.260	4	14400	46	25
2	6070	blue	2017-01-05	10:41:43.0	+08:42:32.20	+19:06:28.27	3	9285	39	27
3	13036	blue	2017-01-18	08:54:37.0	+08:38:00.14	+19:13:29.25	2	4028	39	22
4	14030	blue	2017-01-19	07:37:29.0	+08:38:00.12	+19:13:32.84	2	6436	42	27
5	21084	blue	2017-02-02	07:47:06.0	+08:42:32.65	+19:06:29.63	2	7200	38	26
6	21086	blue	2017-02-02	10:13:11.0	+08:38:00.97	+19:13:30.30	2	8100	45	26
7	22081	blue	2017-02-03	07:48:29.0	+08:42:36.24	+20:10:01.95	5	17400	34	25
8	36069	red	2017-02-21	02:47:19.0	+08:39:37.41	+20:09:57.23	4	14400	53	25
9	36073	red	2017-02-21	07:10:48.0	+08:38:00.12	+19:13:30.54	4	14400	51	25
10	37050	red	2017-02-22	02:46:01.0	+08:36:31.67	+20:17:58.31	4	14400	31	24
11	37055	red	2017-02-22	07:26:14.0	+08:44:27.98	+19:05:08.42	4	13500	28	25
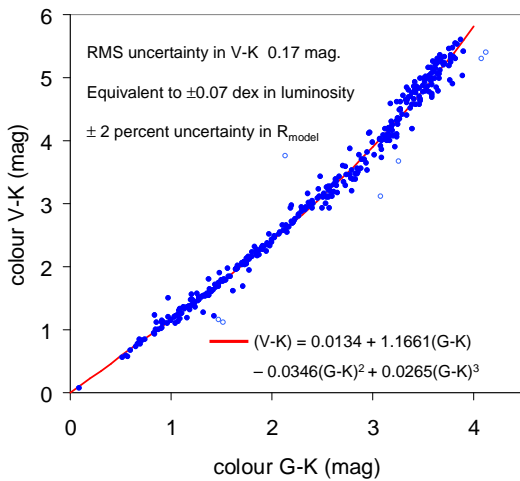
Figure 2. Colour colour plot for targets in Praesepe with reported values of V, G and $K_{2\mathrm{MASS}}$ magnitudes. The red line shows the fitted cubic relation between the two colours. This relation is used to estimate the $V - K$ for Praesepe targets with no reported V magnitude.
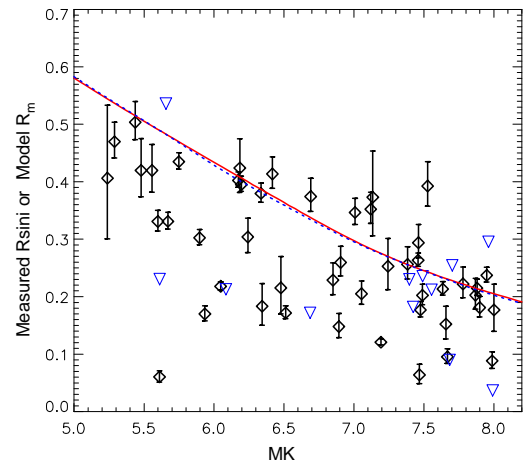

Figure 3. Projected radii, $R \sin i$ (in solar units), vs M_K for low mass stars in Praesepe. Diamonds show targets with $R \sin i$ uncertainties $\leqslant 30$ per cent. Triangles show upper limit values for targets with larger uncertainties. Solid and dashed lines are predictions from 625 Myr BHAC15 and Dartmouth (Dotter et al. 2008) solar metallicity isochrones respectively.

Table 2. Properties of observed science targets in the Praesepe. Periods are from Douglas et al. (2017), BC_K, $\log L/L_\odot$, $M/M_\odot$ and $R/R_\odot$ and a *predicted* $(v\sin i)_p$ are estimated using a BHAC15 model isochrone - see section 2.1. A sample of the table is given here, the full table is made available electronically.

Target name (2MASS)	RA (J2000)	Dec	K_{2MASS} (mag)	$(V-K)_0$ (mag)*	source (V-K)	Period (days)	BC_K (mag)	$\log L/L_\odot$	$M/M_\odot$	$R/R_\odot$	$(v\sin i)_p$ (km s^{-1})
J08355651+2037070	08 35 56.510	+20 37 07.03	14.08	5.78	Gmag	1.22	2.82	-2.33	0.20	0.215	7.0
J08360242+1904265	08 36 02.423	+19 04 26.52	14.25	5.52	Gmag	0.33	2.79	-2.38	0.19	0.206	24.8
J08364501+2008459	08 36 45.016	+20 08 45.90	13.78	5.30	Gmag	2.23	2.77	-2.19	0.24	0.246	4.4
J08364895+1918593	08 36 48.959	+19 18 59.35	11.95	4.63	Vmag	1.17	2.67	-1.42	0.51	0.471	16.0
J08365162+1850193	08 36 51.627	+18 50 19.31	13.48	5.35	Gmag	2.06	2.77	-2.07	0.28	0.271	5.2
J08393071+1856533	08 39 30.714	+18 56 53.40	13.84	5.40	Gmag	1.04	2.78	-2.22	0.23	0.239	9.1
J08395128+2034499	08 39 51.288	+20 34 49.97	11.59	4.62	Vmag	1.84	2.67	-1.27	0.56	0.517	11.2

* $(V-K)_0$ colour estimated from G-K$_{2MASS}$ colour where no V magnitude is available (see section 2.1).

were rebinned to a common wavelength range and sky subtracted using median sky spectra weighted according to the measured fibre efficiencies. Spectra from repeat exposures, after heliocentric velocity correction, were then stacked to produce final target spectra covering a wavelength range 7681–8095Å in 0.1Å steps.

2.4 Radial velocity and projected equatorial velocity

The estimation of radial velocity (RV) and projected equatorial velocity ($v\sin i$) was achieved by cross correlating target spectra with template spectra from the UVES atlas (Bagnulo et al. 2003, see Table 3) after truncation shortward of 7705Å to exclude strong telluric features. The adopted methods were similar to those described in Paper I: RV and $v\sin i$ were determined from the peak and FWHM of a Gaussian profile fitted to the cross-correlation function (CCF). The increase in FWHM with respect to that determined for a set of slowly rotating stars of similar spectral type (FWHM$_0$) was calibrated by artifically broadening the spectra of bright standard stars (see Table 3). Independent calibration curves were determined for the red- and blue-fibre setups.

The precision of RV, FWHM and $v\sin i$ measurements were calculated according to equations (2)–(4) derived in Paper I, where the measurement precision is defined as the product of a scaling factor S and a t-distribution with ν degrees of freedom. The constants used in these expressions were determined empirically from repeated observations of 174 targets in the Pleiades and Praesepe taken with blue fibres. There were too few repeat observations made with red fibres to make an independent estimate of the constants in the scaling formulae so the same values were adopted. This is acceptable since the principal difference between spectra measured using the red and the blue fibres is the change in resolution and this is already accounted for by the presence of FWHM and FWHM$_0$ in the scaling formulae.

Table 4 gives the weighted (by S^{-2}) mean RV and $v\sin i$ values, and their estimated uncertainties, for 230 independent targets in Praesepe. The RVs are measured relative to the median RV; no attempt to provide an absolute RV calibration was made. The dispersion of the relative RVs for red and blue fibres estimated from the median absolute dispersion (MAD) of the target RVs, are $\sim$1.0 km s^{-1} and $\sim$1.5 km s^{-1} respectively (using the approximate relation $\sigma_t =$MAD/0.68 for a t-distribution with $\nu = 4$). These values represent the combined effects of (a) intrinsic dispersion in the cluster, (b) measurement uncertainties and (c) the effects of binarity and are therefore upper limits to the intrinsic velocity dispersion of targets within the cluster.

Table 3. Calibration standards used as cross-correlation function (CCF) templates to determine RVs (see section 2.4). Spectra of the $v\sin i$ standard stars were used to define calibration curves of $v\sin i$ versus the increase in FWHM relative to the value measured for slowly rotating stars, FWHM$_0$, for the blue and red fibres respectively.

No.	M_K range	CCF template	$v\sin i$ standards	FWHM$_0$ (km s^{-1}) blue	red
1	>5.5	HD 34055	Gl 133/Gl 285	24.20	21.30
2	4.9 - 5.5	HD 130328	Gl 133/Gl 285	24.80	22.35
3	4.4 - 4.9	HD 156274	Gl 184/Gl 205	33.35	26.90

3 COMPARISON OF MEASURED RADII WITH CURRENT EVOLUTIONARY MODELS

Equation 1 is used with the measurements of P and $v\sin i$ in Table 4 to estimate $R\sin i$ for targets with $|RV_{\rm rel}| < 10$ km s^{-1} and $(v\sin i)_p > 8$ km s^{-1}. The uncertainty in $R\sin i$ is estimated from the uncertainty in $v\sin i$, which is much greater than the uncertainty in P, giving a *fractional* uncertainty in $R\sin i$ of $S_{v\sin i}/v\sin i$. For targets where this fractional uncertainty is greater than 0.3, upper limits to $R\sin i$ are calculated from P and the upper limit to $v\sin i$. Figure 3 shows $R\sin i$ versus M_K and predicted model radii R_m from the BHAC15 and Dartmouth evolutionary codes (Dotter et al. 2008) for 625 Myr solar metallicity isochrones. These models are almost indistinguishable at this age and in this luminosity range. Figure 4a shows the same data normalised to the BHAC15 model radii as a function of luminosity. The ratio of projected radius to model radius at the target luminosity, $r\sin i = R\sin i/R_m$, is referred to hereafter as the "normalised radius". There are 48 targets that have a fractional uncertainty in $r\sin i$ of $\leqslant 0.3$. A further 12 targets have $r\sin i$ upper limits and are treated as left-censored data.

A maximum likelihood method was used to determine the average over-radius $\rho = R/R_m$, relative to the BHAC15 model radii as a function of luminosity, that best matches the observed data in Fig. 4a. The method is described fully in Paper I, but in brief consisted of using Monte Carlo realisations for each target that assume a random alignment of spin axes. The uncertainties estimated for each target were used along with a treatment of unresolved binarity (described in Appendix 1) and an appropriate treatment of left-censored data, to produce a probability distribution of $r\sin i$ for each target given its luminosity and period and a value of ρ. The best-fitting value of ρ was determined by maximising the log-likelihood function summed over all targets ($\ln \mathscr{L}$). The uncer-

Table 4. Estimated values of relative RV, $v\sin i$ and $R\sin i$ (from Eqn. 1). Absolute uncertainties in RV and $v\sin i$ (defined according to Eqns. 2 and 4) are also given. $R\sin i$ values are shown where $(v\sin i)_p > 8\,\mathrm{km\,s^{-1}}$. Where the relative uncertainty in $v\sin i$ is > 30 per cent, an upper limit is shown along with corresponding upper limits in $R\sin i$. A sample of the Table is shown here, the full version is available electronically.

| Target name (as 2MASS)	M_K (mag)	$\log L/L_\odot$	Period (d)	SNR	RV_{rel} (km s^{-1})	S_{RV} (km s^{-1})	$v\sin i$ (km s^{-1})	$S_{v\sin i}$ (km s^{-1})	$R\sin i$ ($R_\odot$)
J08355651+2037070	7.73	-2.33	1.22	22	-0.80	1.19	10.4	2.0	—
J08360242+1904265	7.90	-2.38	0.33	10	0.40	3.65	27.7	2.4	0.181
J08364501+2008459	7.43	-2.19	2.23	15	0.50	4.87	14.0	6.2	—
J08364895+1918593	5.60	-1.42	1.17	140	1.33	0.51	14.3	0.7	0.331
J08365162+1850193	7.13	-2.07	2.06	27	2.28	0.91	7.6	5.0	—
J08393071+1856533	7.49	-2.22	1.04	26	0.60	2.03	9.0	4.3	<0.162
J08395128+2034499	5.24	-1.27	1.84	69	0.06	0.58	11.2	2.9	0.407
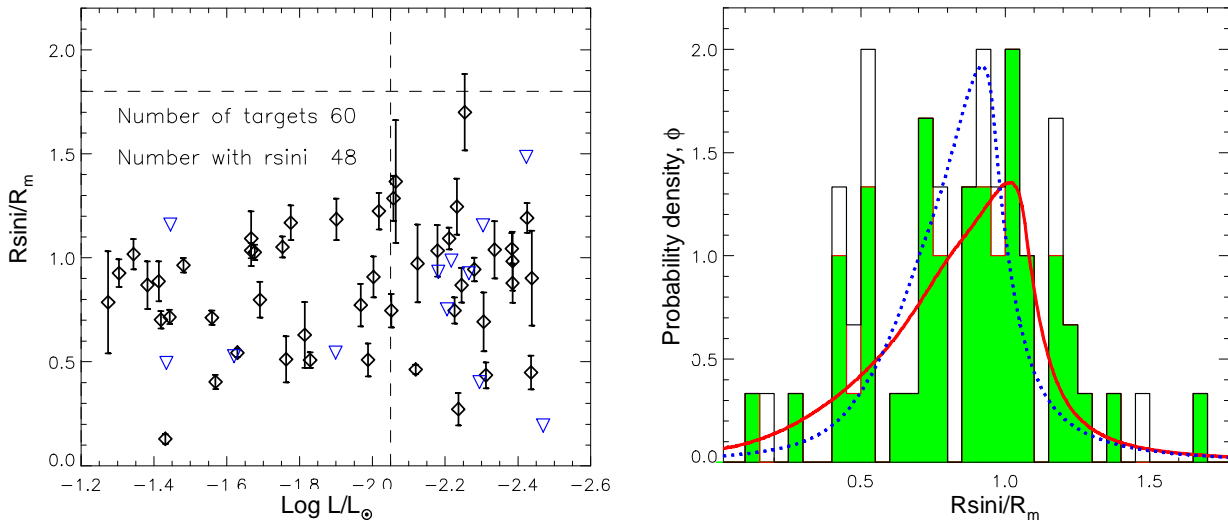
Figure 4. Normalised radii of low mass stars in Praesepe. Plot (a) shows $r\sin i$ as a function of luminosity. Diamonds show $r\sin i$ for targets with a relative uncertainty $\leqslant 30$ per cent. Triangles show upper limits for targets $(v\sin i)_p > 8\,\mathrm{km\,s^{-1}}$ with higher levels of uncertainty. Plot (b) shows the number density of targets as a function of $r\sin i$. Targets with a relative uncertainty $\leqslant 30$ per cent are shown as a solid histogram. The open histogram including the stars with upper limits at their upper limit values. The dotted line shows a model distribution with no over-radius (using BHAC15 model radii and a random distribution of stellar spin-axis orientation). The solid line shows the maximum likelihood model for the best-fitting over-radius of $\rho = 1.07 \pm 0.03$.

tainty in ρ is estimated from the standard deviation of the likelihood function.

Figure 4b shows the number density of targets versus $r\sin i$ compared with what would be expected from a similar set of measurements if the stars have random spin-axis alignment and radii as predicted by the BHAC15 isochrone ($\rho = 1$, shown as a dotted line). The solid line shows the best-fitting model with $\rho = 1.07 \pm 0.03$ (see section 4).

4 RESULTS

4.1 Over-radius with no correction for binarity or metallicity

Figure 5 shows the measured period versus luminosity for targets with $\log L/L_\odot < -0.2$, indicating those stars for which we obtained spectroscopy and those stars which were included as part of the $r\sin i$ analysis (those with $(v\sin i)_p > 8\,\mathrm{km\,s^{-1}}$). The data were split into two luminosity bins for analysis, spanning the approximate mass range $0.15 < M/M_\odot < 0.6$, with roughly equal numbers of targets per bin. The parent sample of the lower luminosity bin contains almost exclusively faster rotating stars with $P < 3$

days. The upper bin includes both stars in the fast rotating "C sequence" and stars in transition between the faster "C sequence" and slower "I sequence" defined for F-K stars by Barnes (2007). Note however, that even the slowest rotating stars that contribute to the $r\sin i$ analysis in both bins have $P < 2$ days. There are too few stars with $(v\sin i)_p > 8\,\mathrm{km\,s^{-1}}$ to make a useful estimate of over-radius at higher masses/luminosities.

The results of the maximum likelihood analysis are shown in Table 5. The estimated over-radius relative to the *solar metallicity* BHAC15 evolutionary model *with no correction made for binarity* is $\rho = 1.07 \pm 0.03$ (or an over-radius of 7 ± 3 per cent). The best fitting model $r\sin i$ distribution is shown in Fig. 4. A model with a free value of ρ is preferred to one with $\rho = 1$. The difference in log likelihood is 2.1 but with an additional free parameter; assuming Wilks' theorem, a likelihood ratio test suggests that the null hypothesis of no radius inflation can only be rejected with a p-value of 0.04 (i.e roughly 2-sigma). Results are also shown when the targets are split into the two luminosity bins. A small radius inflation is favoured over a model with no inflation for each bin, but only at a marginal significance level.

Table 5. The maximum likelihood value of over-radius ρ, for faster rotating low mass stars (with $(v \sin i)_p > 8 \text{ km s}^{-1}$) in Praesepe, relative to radii predicted for a 625 Myr BHAC15 model. N_{targ} is the number of targets included and N_{rsini} is the number of those targets with measured values of $r \sin i$. The column labeled $\Delta \ln \mathscr{L}_{\text{max}}$ gives the increase in log-likelihood with respect to a model (with no free parameters) that assumes ρ=1 and random spin-axis orientation. In the lower portion results are shown for a model with super solar metallicity and including a treatment of unresolved binary stars (see Appendix 1). The errors in ρ are solely the statistical uncertainties. The final row gives the results assuming the non-random spin-axis distribution found by Kovacs (2018); in this case the change in log-likelihood is with respect to our best fitting model with a random axis orientation, that has $\rho = 1.06 \pm 0.04$.

|	N_{targ}	N_{rsini}	$\log L/L_{\odot}$	$\overline{r \sin i}$	$\Delta \ln \mathscr{L}_{\text{max}}$	ρ
Fixed binary fraction = 0, model [FEH]=0						
All targets	60	48	-1.953	0.86	2.1	1.07±0.03
Lower luminosity bin 1	30	22	-2.268	0.916	1.2	1.09±0.05
Upper luminosity bin 2	30	26	-1.639	0.813	1.0	1.06±0.04
Variable binary fraction, model [Fe/H]=0.156						
All targets	60	48	-1.953	0.860	1.1	1.06±0.04
Lower luminosity bin 1	30	22	-2.268	0.916	1.2	1.09±0.05
Upper luminosity bin 2	30	26	-1.639	0.813	0.3	1.03±0.05
Slower rotators (bin 1 P>0.5 d, bin 2 P>1.1 d)	30	22	-1.948	1.007	3.8	1.14±0.04
Faster rotators (bin 1 P<0.5 d, bin 2 P<1.1 d)	30	26	-1.959	0.737	0.3	1.02±0.04
Higher amplitude light curves(amp > 0.038 mag)	31	26	-2.006	0.948	3.8	1.12±0.04
Lower amplitude light curves (amp < 0.038 mag)	29	22	-1.897	0.757	2.2	0.96±0.03
All targets - partial alignment of stellar axes (see Section 5.1)	60	48	-1.953	0.86	-21.8	0.97±0.03
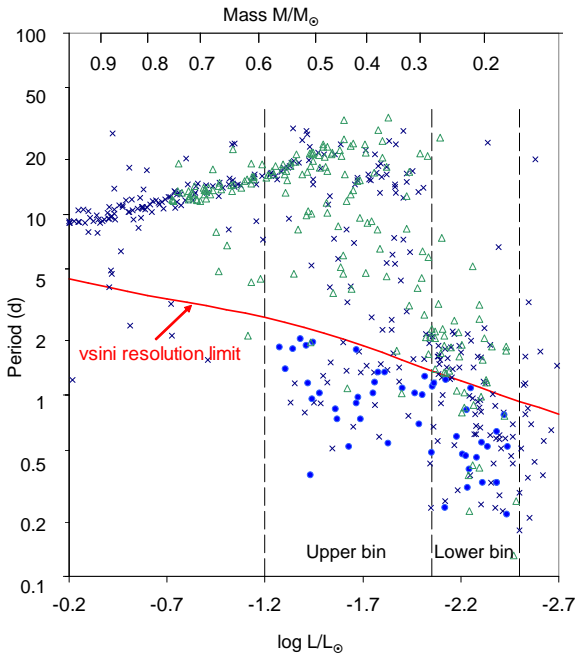
Figure 5. The rotation periods of low mass stars in Praesepe. Triangles mark stars with measured spectra; Filled circles are the subset of stars with measured $r \sin i$ values with uncertainty $\leqslant$ 30 per cent. Crosses show other stars with measured periods reported by Douglas et al. (2017a) but *not* included in our observations. The red line marks the locus of stars with $(v \sin i)_p = 8 \text{ km s}^{-1}$; stars above this line are excluded from the $r \sin i$ analysis. Dashed vertical lines are boundaries that define the upper and lower luminosity bins.

4.2 The binary fraction of targets with measured $r \sin i$

The presence of unresolved binaries in the sample with measured $r \sin i$ affects the inferred ρ in two ways (see Paper I). First, the CCF may be broadened by any unresolved velocity difference between the two components that contribute to the spectrum, leading to an over-estimate of $r \sin i$. Second, because the system luminosity is larger than that of the primary alone, the model radius is systematically over-estimated in binary systems and hence $r \sin i$ is under-estimated. Appendix 1 describes a detailed simulation that is used to provide a correction for these effects, but this requires an estimate of the fraction of unresolved binaries in the population.

Figure 6a shows luminosity versus $(V - K)_0$ for the Praesepe targets. The faster rotating stars, those with measured $r \sin i$ values, appear to lie redward of other Praesepe targets on average, suggesting that the sample used to evaluate ρ may contain a larger proportion of unresolved binary systems than the cluster as a whole. This is not the only possible explanation of a bias in $V - K$, for example in section 5.2 the possibility that large proportions of the stellar surfaces are covered by cool starspots is discussed, but it would be consistent with the conclusion of Douglas et al. (2017) that a high proportion of faster rotating Praesepe stars with $M > 0.3 M_{\odot}$ are probable binaries and also has the largest effect on our inference of the over-radius.

Figure 6b shows the offset in $(V - K)_0$ as a function of luminosity, relative to an average value defined by cubic polynomial fits to the data in each luminosity bin. Also shown in Fig. 6b is the distribution of these offsets for a simulated population with a binary fraction, $B_f = 0.30$ (Duchêne & Kraus 2013), and a Gaussian uncertainty of 0.2 mag in $(V - K)_0$. The simulation draws from a uniform distribution of mass ratios between 0.1 and 1 for the binary stars (Raghavan et al. 2010) and uses the BHAC15 model to estimate colour at a given mass.

Figure 6c compares the cumulative distribution functions (CDFs) of the offsets in Fig. 6b. The CDF for all targets with measured periods is well-described by the Monte-Carlo simulation. The CDFs for the subsets of stars with measured values of $r \sin i$ are poorly described by the simulation with $B_f = 0.30$. A better estimate of B_f can be obtained by using Monte Carlo simulations to determine the probability of a target being a binary as a function of $(V - K)_0$. This yields an average $B_f = 0.47$ for the targets with $r \sin i$ in the upper luminosity bin, and $B_f = 0.38$ for those in the lower luminosity bin. Whilst this is only an approximate method for estimating the binary fraction for the subset of data with measured $r \sin i$, it is acceptable when used to assess the effects of binarity on ρ which is itself a relatively small correction.
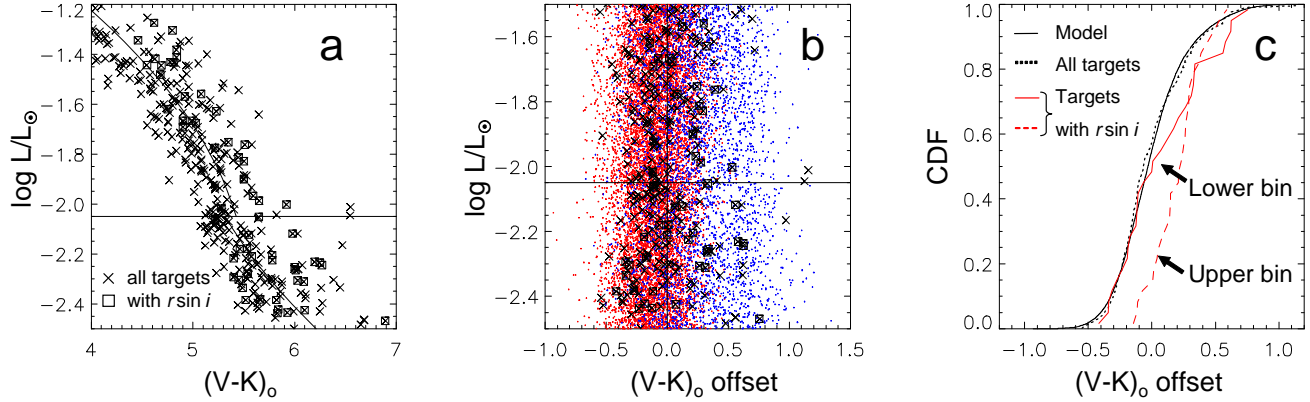
Figure 6. Plot (a) shows $(V - K)_0$ for the Praesepe stars with measured periods in the upper and lower luminosity bins (delineated by the horizontal line). Squares are stars with a measured $r \sin i$, crosses are other targets, the trend lines are cubic polynomial fits to the data in each luminosity bin. Plot (b) shows the offset in $(V - K)_0$ relative to the trend lines in plot (a). Dots show a Monte-Carlo model distribution of single stars (red) and binary stars (blue) for a model with a binary fraction of 0.3 and a measurement uncertainty of 0.2 in $(V - K)_0$ (see Section 4.2). Plot (c) compares the cumulative distribution functions (CDFs) of the $(V - K)_0$ offset shown in plot (b) for all data (black dotted line) and and for just the data with measured $r \sin i$ (red solid and dashed lines for the lower and upper luminosity bin respectively) to the CDF of the Monte-Carlo model data shown as a back solid line.

4.3 The effects of binarity and metallicity on over-radius

Appendix 1 describes the Monte-Carlo model used to estimate the effects of unresolved binarity on the inferred ρ. Including the effects of binarity, assuming the binary frequencies estimated in the previous subsection, a period distribution appropriate for field stars and a flat mass-ratio distribution *increases* the estimated ρ in the Praesepe sample by just 1 per cent. If some of the redward displacements seen in Fig. 6 are in fact caused by spottedness rather than binarity, then the binary fraction will be lower and the influence on ρ will be smaller.

Praesepe has a super-solar metallicity; [Fe/H]= $+0.156 \pm 0.004$ (Cummings et al. 2017). In general, evolutionary models (Baraffe et al. 1998, Dotter et al. 2008) show an increase in radius at fixed luminosity with increasing metallicity. Since BHAC15 models at alternative metallicities are not available, the effect of metallicity on the model radii is estimated from the Dartmouth model radii for [Fe/H]=0 and [Fe/H]=0.16 (Dotter et al. 2008). These models showed an average increase in radius of 2.0 per cent at the higher metallicity (at an age of 600 Myr, over the range $-2.5 < \log L/L_\odot < -0.6$). At the measured Praesepe metallicity this corresponds to a 2 per cent increase in the model radius over the solar metallicity values and hence a uniform *decrease* in ρ of -0.02.

Table 5 shows the estimated value of ρ for fast rotating stars in Praesepe after accounting for the effects of both binarity and super-solar metallicity, assuming a binary fraction of 38 per cent for targets in the lower luminosity bin and 47 per cent for targets in the upper bin. The net effect is to decrease the over-radius by just ~ 1 per cent compared with the value inferred assuming a solar metallicity and no unresolved binaries. The effects on the lower and upper luminosity bins are slightly different. At lower luminosities ρ is almost unchanged, whilst for the upper luminosity bin ρ is decreased by -0.03.

4.4 Effects of light curve amplitude and rotation rate.

Table 5 also compares ρ determined for subsets of the fastest and more slowly rotating stars and for targets showing higher and

lower levels of light curve modulation (reported in Douglas et al. 2017). In each case, the samples were chosen by splitting each of the two luminosity bins at their median rotation period and light curve amplitude respectively. The slower rotating stars have $\rho = 1.14 \pm 0.04$, a much more significant result, with a p-value of 0.002 with respect to a model with no inflation. On the contrary, the fastest rotating stars show little evidence for inflation and an over-radius that is significantly lower. Targets that exhibited a higher level of light curve modulation (above the median value of 0.038 mag) also display evidence for significant inflation (a p-value of 0.001) and have a ρ that is is higher than targets with lower levels of light curve modulation, which do not evidence significant radius inflation.

The difference in ρ between the low- and high-amplitude rotational modulation subsets is expected, since there should be a strong positive correlation between modulation amplitude and $\sin i$ – analysing these subsets with a random $\sin i$ should lead to an underestimated or overestimated ρ respectively. However, there is no similar bias that can explain why the inferred ρ of the faster and slower rotating subsets should be different. Whilst the uncertainties in the estimated value of ρ for individual bins are large due to the small sample sizes, the trend of higher ρ for slower rotators and for stars exhibiting higher levels of light curve modulation are the same as those seen in the larger sample of Pleiades targets in Paper I.

4.5 Systematic uncertainties in the over-radius

Table 5 gives *statistical* uncertainties in ρ based on the standard deviation of the likelihood function, which in turn are chiefly dependent on the number of targets in the analysed sample. Other systematic uncertainties were discussed in Paper I including uncertainty in cluster properties, the effect of surface differential rotation (SDR) and bias due to selection effects in the period data.

For Praesepe the uncertainties in ρ due to uncertainties in age and reddening are negligible. The uncertainty in distance modulus $(M - m)_0$ is ± 0.04 mag, assuming a possible 0.1 mas remaining systematic uncertainty in the mean parallax (Gaia collaboration 2018). This yields an additional uncertainty of ∓ 0.014 in ρ. Whilst
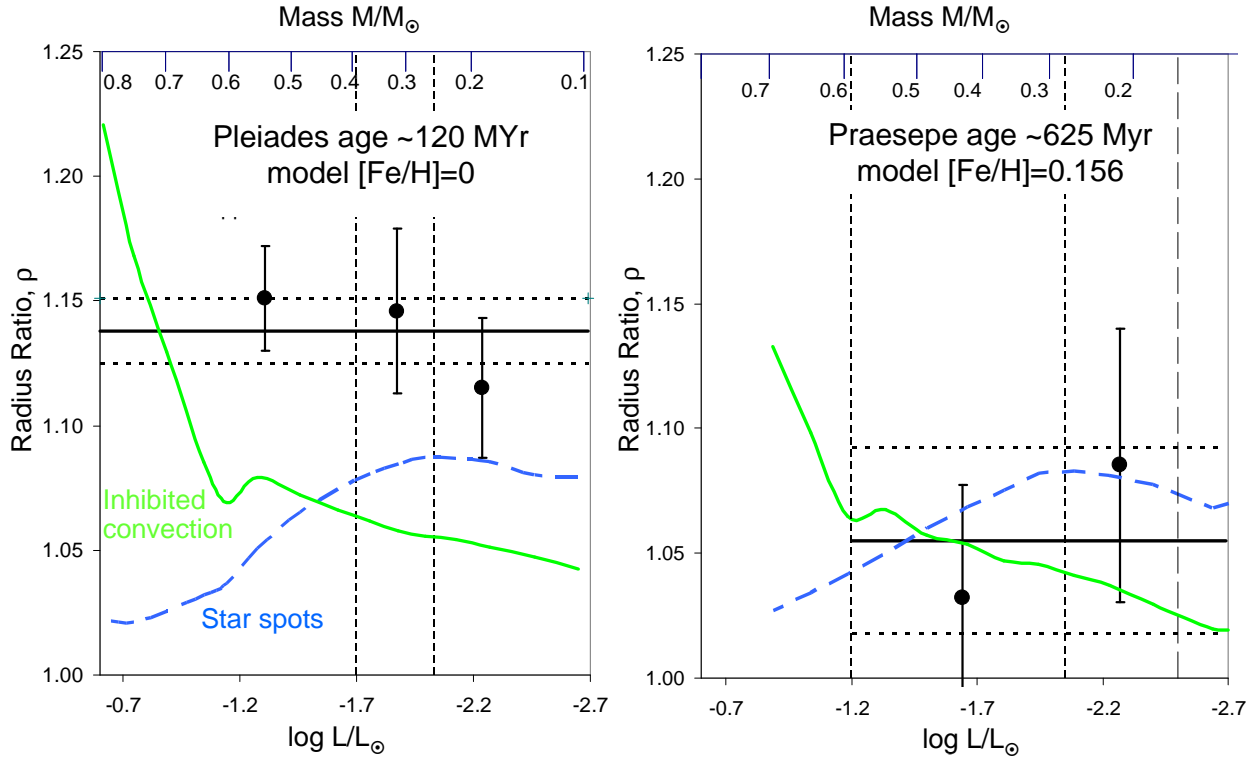
Figure 7. The estimated over-radius of fast rotating low mass stars in the Pleiades and Praesepe relative to the model predictions of BHAC15 at the cluster age. Results in Plot (a) are reproduced from Paper I; results in Plot (b) are from results reported in this paper. Horizontal lines show the mean over-radius, for all the data, with dashed lines indicating the 1-sigma confidence interval. The individual points with error bars show the mean over-radius and uncertainties for stars in luminosity/mass bins. The mass scale at the top of the plot is based on the same BHAC15 model. Green solid lines shows the predicted effect of radius inflation due to magnetic inhibition of convection (Feiden et al. 2015); the blue dashed lines show the predicted effect of starpots with an effective dark spot coverage of $\beta = 0.16$ (see section 5.2).

the estimated metallicity of the cluster is quite consistent between studies (Cummings et al. 2017, Yang et al. 2015, Boesgaard et al. 2013) it is less certain how super-solar metallicity affects stellar radius at a fixed luminosity. Similarly the correction made for binarity in Appendix 1 is approximate. Making a conservative assumption that the corrections made for metallicity and binarity are each accurate to ± 50 per cent gives uncertainties in ρ of only ± 0.01 and ± 0.008 respectively. It was shown in Paper I that SDR had little effect (< 1 per cent) on the measured periods of fast-rotating low mass stars and it is neglected here.

Any bias due to selection effects in period measurement depends on the completeness of the period data; i.e. whether the sample with measured periods are representative or preferentially excludes targets with low inclinations. Selecting only the 50 per cent of Praesepe targets with the largest light curve amplitude would increase the estimated value of ρ by $+0.06$ compared to an analysis of the entire sample (see Table 5), presumably because this sample contains stars with that are heavily biased towards higher $\sin i$. This is an extreme case; Douglas et al. (2017) reported periods for 86 per cent of the Praesepe targets in the luminosity range considered here. Even if the missing 14 per cent of targets without periods were exclusively at the low end of the $\sin i$ distribution, the inferred ρ would be over-estimated by just $+0.01$.

A final source of systematic error would be if the rapid rotation of the stars caused them to be sufficiently oblate to compromise either the calculated model radii or the $v \sin i$ measurements. An

assessment of this effect can be made using equation 46 and the coefficients in table 7 provided by Chandrasekhar (1933) for the equilibrium configuration of rotating polytropes. Taking an extreme example of a fully convective $0.3 M_{\odot}$ star with a rotation period of 0.2 d (see Fig. 5) and a central density of ~ 100 g cm^{-3}, the predicted increase in equatorial radius is just 1.1 per cent. This will be an upper limit to the consequent increase in measured $v \sin i$, since the radius at higher latitudes is smaller, so we conclude that this effect can be neglected.

Thus overall, any additional systematic uncertainty is likely to be ~ 2 per cent and smaller than the existing statistical uncertainties listed in Table 5.

5 DISCUSSION

5.1 The dependence of radius inflation on age, mass and rotation

The main aim of this investigation was to measure the radii of low-mass stars in Praesepe and to compare them with the predictions of evolutionary models and also to compare any over-radius with that estimated for stars of similar mass in the Pleiades using the same analysis methods and very similar data.

The inferred over-radius for this sample of relatively fast-rotating stars in Praesepe is 6 ± 4 percent (after correction for metallicity and binarity, see Table 5) with an additional ~ 2 percent of
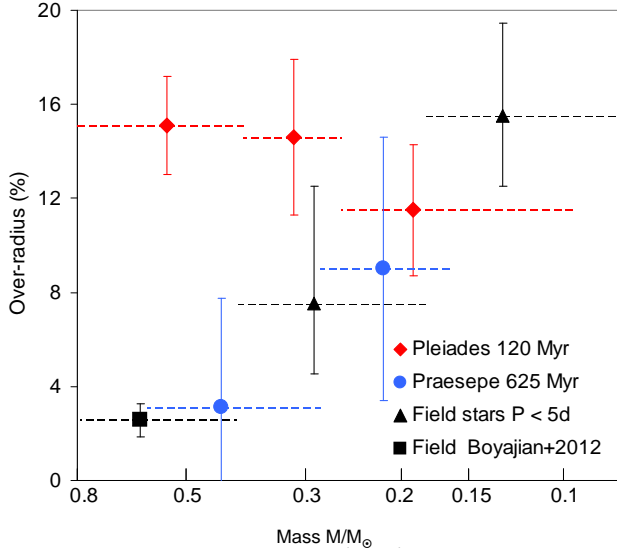
Figure 8 collates these over-radius measurements into one plot and adds higher mass stars with interferometric radii from Boyajian et al. (2012). The masses here are estimated from the BHAC15 models, assuming an age of 5 Gyr for the field stars, and the over-radii are with respect to BHAC15 predictions for the Pleiades, Praesepe and interferometric samples, and with respect to the Dartmouth models for the sample from from Kesseli et al. (2018). Kesseli et al. (2018) reported that the lowest mass stars in their sample (estimated to be $\sim 0.1 M_\odot$ using non-magnetic evolutionary models) are marginally more inflated (15.5^{+4}_{-3} per cent) with respect to the model predictions than stars of higher mass (7.5^{+5}_{-3} per cent inflation for stars with $0.18 < M/M_\odot < 0.4$). Our lowest mass targets in the Pleiades and Praesepe are intermediate to these samples in both mass and estimated over-radius. Figure 8 suggests, albeit strongly based on the Pleiades data, that the decrease in ρ between the age of the Pleiades and the Praesepe/field-star samples is driven by changes for stars with $M > 0.25 M_\odot$, but that there may be no decrease for lower mass stars.

It should be noted that the masses quoted here are derived from standard model-dependent mass-luminosity relationships. In section 5.2 we consider whether models featuring magnetic inhibition of convection or starspots may provide better descriptions of the data and this may change the mapping of luminosity to mass for different groups of stars. However, *all* of the stars in the samples shown in Fig. 8 are strongly magnetically active apart from the sample of nearby field stars with interferometric radii. The increase in inferred mass, at a given luminosity and at ages $\geqslant 100$ Myr, compared with non-magnetic models is at most $+0.05 M_\odot$ for any of the magnetic models considered in section 5.2 and so should not greatly compromise any comparisons between samples divided on estimated mass bins that are much broader than this.

Kesseli et al. (2018) also reported that they find no significant difference in inflation for the fast versus slow rotators, although the comparison is between inflation determined from their fast-rotating sample versus the radii for slower rotating stars determined by other means – either interferometrically (for which there are only a couple of examples at a comparable mass) and for the components of one slowly rotating eclipsing binary system. On the contrary we find, by dividing our sample of stars at their median period, that the fastest rotating stars in our sample, are *less* inflated than those with slower rotation by 12 ± 6 per cent (see Table 5), although all of these stars are easily rapidly rotating enough to have saturated levels of magnetic activity. For example, the stars in our Praesepe sample have $(V - K)_0 > 4$ (see Fig. 6), and corresponding convective turnover times of > 50 days (e.g. see Wright et al. 2018). Magnetic saturation as judged by coronal X-ray and chromospheric emission appears to set in below Rossby numbers (rotation period/convective turnover time) of 0.1 at all the spectral types considered here (e.g. Jeffries et al. 2011; Wright et al. 2011, 2018; Newton et al. 2017) and thus all stars with $P < 5$ days are in the saturated regime, which includes all targets used for the $r \sin i$ determinations (see Fig. 5).

In Paper I we suggested that it is the increased radii of these stars that could be *responsible* for their slower rotation rates, rather than the other way around. Angular momentum losses via a magnetically coupled wind may be strongly radius-dependent (Reiners & Mohanty 2012; Matt et al. 2015), or may increase for some other reason in the more inflated stars – perhaps a change in the magnetic field configuration (e.g. Garraffo, Drake & Cohen 2016). If the timescale for significant angular momentum loss becomes shorter than the timescale on which the stellar radius can change, then any decline of observed over-radius with age could be ex-

Figure 8. Composite plot showing the mean over-radius measured on samples of low mass stars from four studies, (a) over-radii of stars in the Pleiades (paper I), (b) over-radii in the Praesepe (this paper), (c) over-radii of faster rotating field stars (Kesseli et al. 2018) and (d) over-radii of slowly rotating field stars (from paper I based on radii reported by Boyajian et al. 2012) as a function of mass determined from stellar luminosities. Vertical error bars show 1σ uncertainties in over-radius. Horizontal dashed lines show the mass range of binned data contributing to each point.

systematic uncertainty. The difference in log-likelihood between a model with no over-radius and the best-fitting model is however not very large; although our measurement is consistent with a small inflation, we cannot be certain at the > 2-sigma level that these stars are bigger (at a given luminosity) than predicted by the most commonly used low-mass evolutionary models that do not account for magnetic effects (Dotter et al. 2008; BHAC15).

Figure 7 makes a comparison of the over-radii measured for the Pleiades (from table 5 in Paper I) and Praesepe. The predicted radii of stars in the Pleiades at 120 Myr are slightly larger than those of similar luminosity in Praesepe at 625 Myr due to the completion of PMS contraction in that interval. Figure 7 has already taken this into account – the over-radii are calculated with respect to models at the appropriate age. In Fig. 7 the mean over-radius of $\rho = 1.14 \pm 0.02$ in the Pleiades is greater than Praesepe at the 2-sigma level; the inclusion or not of the increased metallicity of Praesepe and the effects of unresolved binarity (see Table 5) changes this difference by only ~ 1 percent. The stars in Praesepe are rotating somewhat slower on average than the Pleiades targets from Paper I, however the more slowly rotating half of the Pleiades targets, which are much more comparable to the present Praesepe sample (see table 5 in Paper I), have an over-radius of $\rho = 1.16 \pm 0.03$ and so this does not change any of the discussion above.

The final over-radius estimates of 14 ± 2 per cent for the Pleiades and 6 ± 4 per cent in Praesepe can also be compared with the over-radius of $13^{+3}_{-2.5}$ per cent with respect to the BHAC15 models reported by Kesseli et al. (2018) for a sample of field M-dwarfs with rotation periods less than 5 days. Kesseli et al. (2018) used a very similar analysis technique, but our focus on samples of stars in clusters removes uncertainties associated with the age and metallicity of a field star sample.

plained in terms of a spread in radii. The larger stars would spin down more rapidly, and since the sample of stars for which we can measure $r \sin i$ is strongly biased towards the most rapid rotators, then the more inflated stars would preferentially be excluded in older samples. The mass-dependence of the over-radii seen in Fig. 8 could then merely be a consequence of the much longer spin-down timescales in lower mass stars – the majority of stars in the lowest luminosity bin of Praesepe are still fast rotators for which a $r \sin i$ measurement is possible, whereas in the higher luminosity bin, more than half have spun down to rotation levels where $r \sin i$ could not be measured in our spectroscopy (see Fig. 5).

5.2 Comparison with magnetic models

A significant over-radius with respect to "standard" evolutionary models has been identified in fast-rotating M-dwarfs in the Pleiades (Paper I) and now (marginally) for the lowest mass stars in Praesepe (this paper) and in a field star sample of very low-mass stars (Kesseli et al. 2018). However, where the data exists (primarily at the upper end of our considered mass range) there is a much better agreement between the same evolutionary models and interferometric radii for field stars of similar mass but lower levels of magnetic activity (e.g. Boyajian et al. 2012), suggesting that magnetic activity may be responsible for the discrepancies. Two flavours of models incorporating the effects of magnetic fields are provided by: (i) magnetic inhibition of convective flux (e.g. Feiden & Chaboyer 2012, 2014) or the blocking of radiative flux from the stellar surface by cool, magnetic starspots (Jackson & Jeffries 2014a; Somers & Pinsonneault 2015a,b).

Magnetic inhibition of convection should become less effective at lower masses as the stars become fully convective, and the effect is also predicted to weaken for older stars that have become established on the main sequence compared with PMS stars (see for example Feiden & Chaboyer 2014; Feiden et al. 2015). Both of these effects are apparent in Fig. 7, where we plot the over-radius (compared to standard models) of a 120 Myr and 625 Myr isochrone from magnetic models that implement magnetic inhibition of convection via a rotational dynamo, with a fixed surface field of 2.5 kG (Feiden et al. 2015). The data from Praesepe alone are possibly consistent with this model. However, the model is inconsistent with the additional data provided by the Pleiades and the older field star sample of Kesseli et al. (2018), both of which show significantly larger over-radii than predicted by the magnetic models, and in the case of the field stars (and perhaps Praesepe too), an over-radius that increases with decreasing mass (see Fig. 8).

A field of 2.5 kG represents an approximate equipartition value for these low mass stars, where the thermal and magnetic pressures in the photosphere are roughly equal. Some recent measurements using the Zeeman effect suggest that average surface magnetic fields may reach strengths of 7 kG, but only in low-mass, fast-rotating, fully-convective stars (Shulyak et al. 2017). The models of Feiden et al. (2015) suggest (see their fig. 2) that the inflationary effect of magnetic fields scales more steeply than linearly and so the mass- and age-dependence of radius inflation might be explained if the lowest mass stars in our Pleiades and Praesepe samples, and the most active fully-convective field stars, host super-equipartition fields that persist for billons of years.

A further alternative could be provided by dark starspots. A large starspot coverage reduces the radiative flux from the surface and results in an over-radius with respect to an immaculate star of the same mass and age. The level of inflation depends on the fraction β of the flux blocked by spots. A second order effect is that

the colours and bolometric correction of the star will be changed depending on both the spot coverage and the ratio of spotted to unspotted surface temperature (e.g. Jackson & Jeffries 2014b). In Paper I we were able to take advantage of spectroscopic observations of the Pleiades low-mass stars, which were modelled with two temperature components by Fang et al. (2016). This revealed a range of β values with a mean of 0.16 for the sample of fast-rotating stars considered there. Figure 7 shows the predicted over-radius due to spots with $\beta = 0.16$, interpolated from the models of Somers & Pinsonneault (2015a). The spot model with this value of β provides a good match to the Praesepe data but is incapable of producing the larger over-radii in the Pleiades, especially at the higher masses/luminosities, without increasing the adopted value of β (or including some additional element of inflation due to suppression of convection).

Unfortunately, there are no spectroscopically determined β values for our Praesepe targets, so it is unknown whether the level of spot coverage changes between the ages of Praesepe and the Pleiades or for older field stars. The median rotation period of the stars certainly does increase, but all stars contributing to the estimate of ρ rotate fast enough to be at saturated magnetic activity levels. As a proxy, we can look at the distribution of light curve amplitudes. For spot coverages less than 50 per cent, it is likely that spot coverage and light curve amplitude will be positively correlated, with amplitude roughly proportional to $\beta^{1/2}$ for spots of a given size and temperature (Jackson & Jeffries 2013), although this relationship would be complicated by any changes in the latitudinal distribution of spots or changes in the mean spot size.

Figure 9 shows a comparison of the cumulative distribution of spot amplitude (defined in the same way) for Praesepe versus the Pleiades, which considers *only* the stars used in the respective $r \sin i$ analyses, split at their median values into faster and slower rotating subsets. The slower rotating half of the Praesepe sample have a larger mean light curve amplitude than the faster-rotating half. A Kolmogorov-Smirnov test suggests a 99 per cent significant difference between the cumulative distributions. This might fit in with an explanation involving radius inflation due to starspots but there is no straightforward way to translate this into a difference in β. The difference between the faster and slower rotating samples in the Pleiades is in the same direction, but is much less significant. There is also no significant decline in light curve amplitudes between the faster rotating subsets in the Pleiades and Praesepe to accompany the observed decrease in ρ.

In conclusion, the results are inconclusive. The mass-dependence that we identify seems inconsistent with the magnetically inhibited convection models with equipartition magnetic fields at the surface. Some fast-rotating, low-mass, fully-convective field stars have been found to host stronger magnetic fields and such fields might be capable of providing the observed mass-dependence. A mass-dependent starspot coverage could also provide this mass-dependence, but there is no strong evidence for a decrease in spot coverage with age that might explain the reduced over-radius among the higher mass stars in Fig. 8. These considerations are complicated by the apparent rotation-dependence of the over-radius, which could be a selection effect cause by the progressive spindown of larger stars and their exclusion from our samples.

5.3 Non-random axis orientation

The analysis so far has made the assumption that there is no preferred orientation of the spin-axes. Recent work by Kovacs (2018) has questioned this assumption, specifically with regard to the Prae-
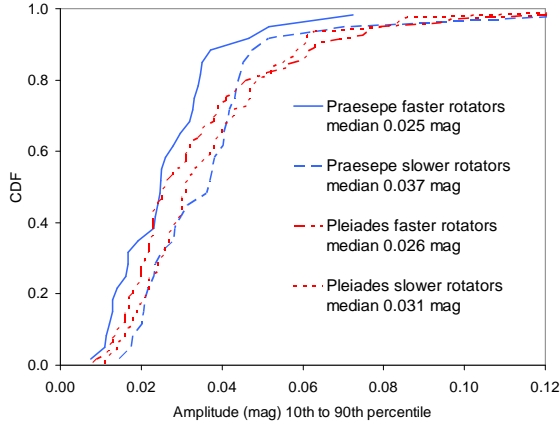
Figure 9. Cumulative distributions of light curve amplitude for stars with measure values of $r\sin i$ in Pleiades (Paper I) and Praesepe (this paper) split into fast and slower rotating subsets.
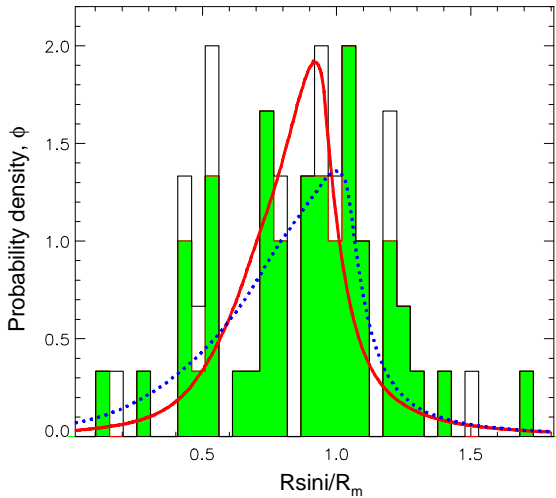

Figure 10. Comparison of the the measured distribution of $r\sin i$ as a function of luminosity with the best fit model distributions found using the maximum likelihood model. The dotted line shows results for a random distribution of stellar spin-axis orientation and $\rho = 1.06 \pm 0.04$. The solid line shows results for a partially aligned distribution with an average inclination of $76°$ distributed over a cone with a half opening angle of $\lambda=47°$ and $\rho=0.97\pm0.03$.

sepe cluster. Using quite similar techniques to those discussed here – rotation periods from Kepler K2 data and literature $v\sin i$ values for 120 F-K dwarfs from Mermilliod, Mayor & Udry (2009) – Kovacs found that for this higher mass stellar sample, the $r\sin i$ distribution was better fitted with a model that had no over-radius but a narrower, aligned $\sin i$ distribution that was characterised with spin-axes at an average inclination of $76°\pm14°$ and distributed over a cone with a half opening angle of $47° \pm 24°$.

We have investigated whether our data are consistent with this model. The results are shown in Table 5 and Fig. 10. The effect of restricting the spin-axes to a cone with this relatively high inclination angle, increases the mean value of $\sin i$ to 0.90. As a result, a much lower value of ρ is required to fit the data and we find $\rho = 0.97 \pm 0.03$, consistent with no over-radius at all. However, the fit to the data is much worse; the narrower range of predicted

$r\sin i$ produced by this model is a poor match to the observed distribution. The difference in log likelihood of -21.8 (see Table 5, with the same number of data points and free parameters) decisively favours the model with a random axis orientation. Indeed the aligned model is disfavoured even versus a model with $\rho = 1$ and a random axis orientation ($\Delta \ln \mathscr{L}$=-19.7).

In Paper I we conducted tests with a range of mean axis inclinations and cone opening angles for the Pleiades sample, concluding that while alignments were possible if the mean inclination angle was $< 45°$, that these would require much higher values of ρ to compensate. Non-random axis orientations with higher mean inclinations were poor fits to the data and were ruled out. We see the same effect in Praesepe for the particular case of an average inclination of $76°$ (and $\lambda = 47°$). In conclusion we can rule out the non-random axis distribution proposed by Kovacs (2018) or any strong alignment with a large mean axis inclination in Praesepe, but weak alignments or strong alignments with a low mean axis inclination (and much larger over-radius) are still possible. It is worth noting however that Corsaro et al. (2017) have suggested, on the basis of numerical simulations, that any residual alignment resulting from the initial angular momentum and cluster formation process, might only be apparent in the higher mass stars of a cluster.

6 SUMMARY

Published rotation periods from Kepler K2 and new measurements of rotational broadening have been combined to estimate projected radii for a set of stars in the Praesepe cluster. Adopting a random distribution of spin-axis orientation and using a maximum likelihood technique, the average radius of these fast-rotating ($P \sim 2$ days or less), low-mass ($0.15 < M/M_\odot < 0.6$) stars is inferred to be 7±4 per cent higher at a given luminosity than predicted by the solar-metallicity isochrones of Baraffe et al. (2015) and Dotter et al. (2008). Allowing for unresolved binarity and the super-solar metallicity of Praesepe reduces the estimated over-radius to 6 ± 4 per cent and perhaps consistent with no inflation at all.

The average over-radius in Praesepe is lower (at a 2-sigma significance level) than the 14 ± 2 per cent measured for a larger sample of targets with similar mass in the younger Pleiades using similar techniques (Jackson et al. 2018). Most of this evolution appears to occur at the higher mass end of the samples, in agreement with the results found for low-mass field stars using similar techniques (Kesseli et al. 2018). The trend of more inflation at lower masses goes against the predictions of models incorporating inhibition of convection by dynamo-generated interior magnetic fields unless the fields are much stronger than equipartition values in lower mass stars. An interpretation involving extensive coverage by starspots may be more consistent with the mass dependence, but there is no evidence that spot coverage declines between the Pleiades and Praesepe in the studied samples. Although the Praesepe targets are slower rotating on average than the previously studied Pleiades, a comparison with the more slowly rotating half of the Pleiades sample does not alter the conclusions above, and measurements for both clusters are based exclusively on stars that rotate fast enough to have saturated levels of magnetic activity.

Another notable feature, that was also observed in the Pleiades, is that the fastest rotating stars in our sample are the *least* inflated with respect to the models. An interpretation of this could be that angular momentum loss is strongly radius dependent (as suggested by Reiners & Mohanty 2012 and Matt et al. 2015) and that larger stars are spun down more rapidly and hence progres-

sively disappear from the analysed samples because they do not spin fast enough for their rotational broadening to be measured.

The main analysis assumes that the orientation of spin axes in the parent sample is random. Recent work on higher mass stars in Praesepe by Kovacs (2018) has suggested a systematic alignment of the spin axes. Such an alignment is ruled out by the relatively broad distribution of projected radii in our sample. Weaker alignments, or alignments with a low mean inclination angle are still possible, but would mean that the over-radius we have found is an under-estimate.

REFERENCES

Bagnulo S., Jehin E., Ledoux C., Cabanac R., Melo C., Gilmozzi R., The ESO Paranal Science Operations Team 2003, The Messenger, 114, 10

Baraffe I., Chabrier G., Allard F., Hauschildt P. H., 1998, A&A, 337, 403

Baraffe I., Homeier D., Allard F., Chabrier G., 2015, A&A, 577, A42

Barnes S. A., 2007, ApJ, 669, 1167

Bershady M., Barden S., Blanche P.-A., Blanco D., Corson C., Crawford S., Glaspey J., Habraken S., Jacoby G., Keyes J., Knezek P., Lemaire P., Liang M., McDougall E., Poczulp G., Sawyer D., Westfall K., Willmarth D., 2008, in Ground-based and Airborne Instrumentation for Astronomy II Vol. 7014 of PSPIE, WIYN bench upgrade: a revitalized spectrograph. p. 70140H

Boesgaard A. M., Roper B. W., Lum M. G., 2013, ApJ, 775, 58

Bouvier J., Barrado D., Moraux E., Stauffer J., Rebull L., Hillenbrand L., Bayo A., Boisse I., Bouy H., DiFolco E., Lillo-Box J., Calderón M. M., 2018, A&A, 613, A63

Boyajian T. S., von Braun K., van Belle G., 2012, ApJ, 757, 112

Carpenter J. M., 2001, AJ, 121, 2851

Chandrasekhar S., 1933, MNRAS, 93, 390

Claret A., Diaz-Cordoves J., Gimenez A., 1995, A&AS, 114, 247

Corsaro E., Lee Y.-N., García R. A., Hennebelle P., Mathur S., Beck P. G., Mathis S., Stello D., Bouvier J., 2017, Nature Astronomy, 1, 0064

Covey K. R., Agüeros M. A., Law N. M., Liu J., Ahmadi A., Laher R., Levitan D., Sesar B., Surace J., 2016, ApJ, 822, 81

Cummings J. D., Deliyannis C. P., Maderak R. M., Steinhauer A., 2017, AJ, 153, 128

Dotter A., Chaboyer B., Jevremović D., Kostov V., Baron E., Ferguson J. W., 2008, ApJS, 178, 89

Douglas S. T., Agüeros M. A., Covey K. R., Kraus A., 2017, ApJ, 842, 83

Duchêne G., Bouvier J., Moraux E., Bouy H., Konopacky Q., Ghez A. M., 2013, A&A, 555, A137

Fang X.-S., Zhao G., Zhao J.-K., Chen Y.-Q., Bharat Kumar Y., 2016, MNRAS, 463, 2494

Feiden G. A., 2016, A&A, 593, A99

Feiden G. A., Chaboyer B., 2012, ApJ, 761, 30

Feiden G. A., Chaboyer B., 2014, ApJ, 789, 53

Feiden G. A., Jones J., Chaboyer B., 2015, in van Belle G. T., Harris H. C., eds, 18th Cambridge Workshop on Cool Stars, Stellar Systems, and the Sun Vol. 18 of Cambridge Workshop on Cool Stars, Stellar Systems, and the Sun, Updating the Dartmouth Stellar Evolution Model Grid: Pre-main-sequence Models Magnetic Fields. pp 171–176

Gaia Collaboration Babusiaux C., van Leeuwen F., Barstow M. A., Jordi C., Vallenari A., Bossini D., Bressan A., Cantat-Gaudin T., van Leeuwen M., et al. 2018, ArXiv e-prints

Gaia Collaboration Brown A. G. A., Vallenari A., Prusti T., de Bruijne J. H. J., Mignard F., Drimmel R., Babusiaux C., Bailer-Jones C. A. L., Bastian U., et al. 2016, A&A, 595, A2

Gaia Collaboration van Leeuwen F., Vallenari A., Jordi C., Lindegren L., Bastian U., Prusti T., de Bruijne J. H. J., Brown A. G. A., Babusiaux C., et al. 2017, A&A, 601, A19

Garraffo C., Drake J. J., Cohen O., 2016, A&A, 595, A110

Hartman J. D., Bakos G. Á., Kovács G., Noyes R. W., 2010, MNRAS, 408, 475

Horne K., 1986, PASP, 98, 609

Jackson R. J., Deliyannis C. P., Jeffries R. D., 2018, MNRAS, 476, 3245

Jackson R. J., Jeffries R. D., 2010, MNRAS, 402, 1380

Jackson R. J., Jeffries R. D., 2013, MNRAS, 431, 1883

Jackson R. J., Jeffries R. D., 2014a, MNRAS, 445, 4306

Jackson R. J., Jeffries R. D., 2014b, MNRAS, 441, 2111

Jackson R. J., Jeffries R. D., Maxted P. F. L., 2009, MNRAS, 399, L89

Jackson R. J., Jeffries R. D., Randich S., Bragaglia A., Carraro G., Costado M. T., Flaccomio E., Lanzafame A. C., Lardo C., Monaco L., Morbidelli L., Smiljanic R., Zaggia S., 2016, A&A, 586, A52

Jeffries R. D., 2007, MNRAS, 381, 1169

Jeffries R. D., Jackson R. J., Briggs K. R., Evans P. A., Pye J. P., 2011, MNRAS, 411, 2099

Jeffries R. D., Jackson R. J., Franciosini E., et al. 2017, MNRAS, 464, 1456

Kesseli A. Y., Muirhead P. S., Mann A. W., Mace G., 2018, AJ, 155, 225

Kovacs G., 2018, A&A, 612, L2

Kraus A. L., Cody A. M., Covey K. R., Rizzuto A. C., Mann A., Ireland M., Jensen E. L. N., Muirhead P. S., 2016, in American Astronomical Society Meeting Abstracts Vol. 227 of American Astronomical Society Meeting Abstracts, The Mass-Radius Relation of Young Stars from K2. p. 236.12

Kraus A. L., Douglas S. T., Mann A. W., Agüeros M. A., Law N. M., Covey K. R., Feiden G. A., Rizzuto A. C., Howard A. W., Isaacson H., Gaidos E., Torres G., Bakos G., 2017, ApJ, 845, 72

Kraus A. L., Hillenbrand L. A., 2007, AJ, 134, 2340

Lanzafame A. C., Spada F., Distefano E., 2017, A&A, 597, A63

López-Morales M., Ribas I., 2005, ApJ, 631, 1120

MacDonald J., Mullan D. J., 2013, ApJ, 765, 126

Matt S. P., Brun A. S., Baraffe I., Bouvier J., Chabrier G., 2015, ApJ, 799, L23

Morales J. C., Ribas I., Jordi C., 2008, A&A, 478, 507

Morales J. C., Ribas I., Jordi C., Torres G., Gallardo J., Guinan E. F., Charbonneau D., Wolf M., Latham D. W., Anglada-Escudé G., Bradstreet D. H., Everett M. E., O'Donovan F. T., Mandushev G., Mathieu R. D., 2009, ApJ, 691, 1400

Mullan D. J., MacDonald J., 2001, ApJ, 559, 353

Newton E. R., Irwin J., Charbonneau D., Berlind P., Calkins M. L., Mink J., 2017, ApJ, 834, 85

Raghavan D., McAlister H. A., Henry T. J., Latham D. W., Marcy G. W., Mason B. D., Gies D. R., White R. J., ten Brummelaar T. A., 2010, ApJS, 190, 1

Reiners A., Mohanty S., 2012, ApJ, 746, 43

Rhode K. L., Herbst W., Mathieu R. D., 2001, AJ, 122, 3258

Shulyak D., Reiners A., Engeln A., Malo L., Yadav R., Morin J., Kochukhov O., 2017, Nature Astronomy, 1, 0184

Skrutskie M. F., Cutri R. M., Stiening R., Weinberg M. D., Schnei-
   der S., Carpenter J. M., Beichman C., Capps R., Chester T., Elias
   J., Huchra J., 2006, AJ, 131, 1163
Somers G., Pinsonneault M. H., 2014, ApJ, 790, 72
Somers G., Pinsonneault M. H., 2015a, ApJ, 807, 174
Somers G., Pinsonneault M. H., 2015b, MNRAS, 449, 4131
Somers G., Stassun K. G., 2017, AJ, 153, 101
Spruit H. C., Weiss A., 1986, A&A, 166, 167
Torres G., 2013, Astronomische Nachrichten, 334, 4
van Leeuwen F., 2009, A&A, 497, 209
Wright N. J., Drake J. J., Mamajek E. E., Henry G. W., 2011, ApJ,
   743, 48
Wright N. J., Newton E. R., Williams P. K. G., Drake J. J., Yadav
   R. K., 2018, MNRAS, 479, 2351
Yang X. L., Chen Y. Q., Zhao G., 2015, AJ, 150, 158

ACKNOWLEDGMENTS

APPENDIX A: BINARY STAR SIMULATIONS

The normalised radius, $r \sin i$ is the ratio of the projected radius, $R \sin i$ to the model radius R_m at the measured luminosity, L. In the case of unresolved binary stars the measured values of both $R \sin i$ and R_m are increased above the true values of the primary star (see Paper I). Depending on the binary frequency and binary properties this can either increase or decrease the estimated value of the over-radius ρ.

A1 Modelling binarity

Our method for modelling the effects of unresolved binarity on the CCF follows that described in Jackson et al. (2016) and depends on the difference in RV between the primary and secondary and their relative contribution to the observed spectrum. The resultant CCF is modelled as the sum of two Gaussian profiles; the first represents the primary star with central velocity $RV + RV_a$ and $FWHM_a$, where RV is the systemic velocity and RV_a is the line-of-sight velocity of the primary relative to the centre of mass; the second represents the secondary with velocity $RV - RV_a/q$ and $FWHM_b$, where q is the binary mass ratio. The resultant $FWHM_s$ of a single Gaussian fitted to this sum can be estimated as a function of RV_a and the ratio of flux contributions from the two stars (which depends on q).

To a reasonable approximation the effect of rotational broadening is to increase the width of the CCF as $FWHM = FWHM_0 \sqrt{1 + (v \sin i/C)^2}$ where $FWHM_0$ is the unbroadened width and C is a constant that is proportional to the resolution of the spectrograph. Using this expression the increase in the measured $(v \sin i)_s$ relative to the true $(v \sin i)_a$ of the primary

is, $C(\sqrt{FWHM_s/FWHM_0 - 1} - \sqrt{FWHM_a/FWHM_0 - 1})$ and hence (from Eqn. 1) the increase in inferred $R \sin i$, relative to that of the primary is given by

$$\frac{(v \sin i)_s}{(v \sin i)_a} = \frac{\sqrt{FWHM_s/FWHM_0 - 1}}{\sqrt{FWHM_a/FWHM_0 - 1}} \qquad (A1)$$

A Monte Carlo model is used to calculate the *average* effect of binarity on ρ as a function of target mass and $v \sin i$ assuming a log normal distribution of binary periods (with $\overline{\log P} = 5.03$ and $\sigma_{\log P} = 2.28$) and a uniform distribution of q between 0.1 and 1 (Raghavan et al. 2010). Typical results are shown in Fig. A1 for a star of primary mass $M_a = 0.5 M_\odot$, a binary fraction of 0.5 and a true equatorial velocity of $v = 15 \, \mathrm{km \, s^{-1}}$. Figure A1a shows the distribution of RV_a relative to the centre of mass and Fig. A1b shows the distribution of $(v \sin i)_s$ for a sample including 50 per cent unresolved binaries (those with $|RV_a - RV_b| < 10 \, \mathrm{km \, s^{-1}}$ for our spectrograph) compared to the distribution of $v \sin i$ for single stars. The net effect is to increase the average value of $v \sin i$ by 3.5 percent and produce a small tail of targets with a measured $v \sin i$ in excess of the true equatorial velocity.

Figure A1c shows the effect of binarity on R_m. For each binary in the simulation we estimate the luminosity of the primary and the system (from M_a and q using BHAC15 model) and use this to calculate the increase in model radius, R_m^s/R_m^a. The distribution shows a tail of stars with $R_m^s/R_m^a > 1$, due to binaries with $q \sim 1$, which increases the average value of R_m by 2.5 per cent and hence decreases $r \sin i$. Figure A1d shows the combined effects of binarity on the base probability density function of $r \sin i$ used in the maximum likelihood analysis. In the absence of binarity and measurement uncertainty the base probability function follows the dotted line (see Eqn. 5 for case of $\rho = 1$). Binarity changes this distribution producing both a tail stars with $\phi > 1$ and a small "bump" at $r \sin i \sim 0.8$ due to binaries with $q \sim 1$.

A2 The effects of binarity on inferred over-radius

The net effect of unresolved binarity on estimates of ρ is not straightforward. The two factors discussed above act in opposite directions and scale differently with $v \sin i$. The increase in ρ due to unresolved binarity increasing the average $v \sin i$ measurement scales as $(v \sin i)_a^{-1}$, whereas the decrease in ρ due to the overestimate of R_m is independent of $v \sin i$. The net effect is that the presence of unresolved binaries in a sample of slowly rotating stars is to increase the inferred ρ above its true value, but binarity in a sample of faster rotating stars will decrease the inferred ρ.

The Praesepe targets with measured $r \sin i$ appear to have relatively high binary fractions (47 and 38 per cent in the upper and lower bins respectively, see Section 4.2), but they are also fast rotators, with a weighted mean $v \sin i \simeq 20 \, \mathrm{km \, s^{-1}}$. Consequently binarity has only a small net effect, leading to an *over-estimate* of ρ by ~ 1 per cent.

This paper has been typeset from a TeX/ LaTeX file prepared by the author.
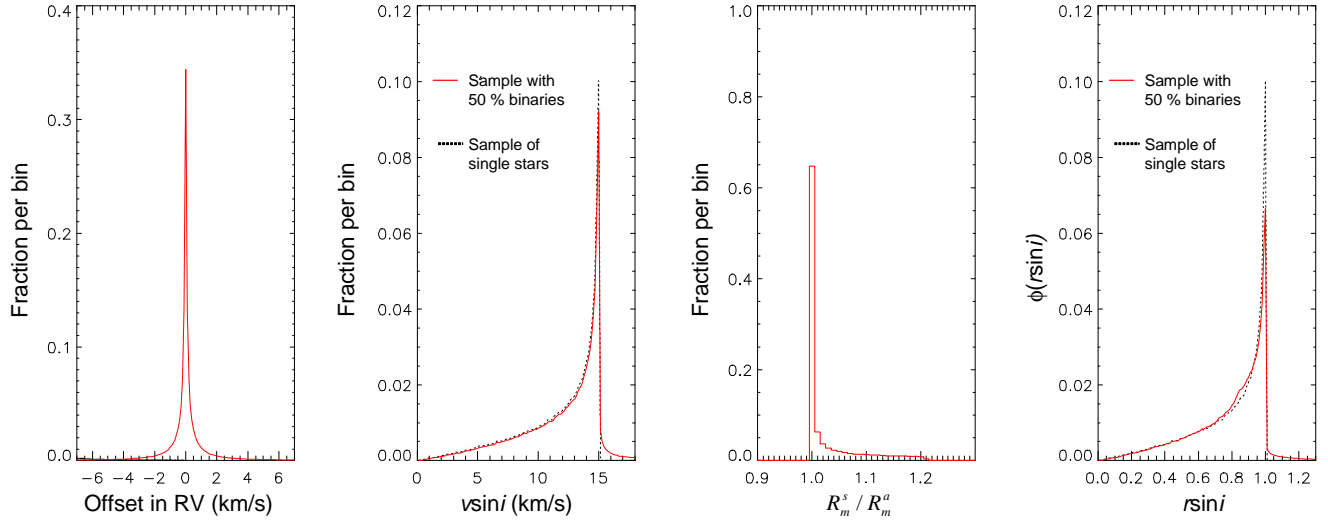
Figure 1. An example of the predicted effects of binarity on a population of stars with mass (of the primary star if binary) $0.5\,M_\odot$, an equatorial velocity of $15\,\mathrm{km\,s^{-1}}$ and a binary fraction 0.5 (see Section A1). (a) The distribution of primary star RV relative to the centre of mass. (b) The distribution of measured $v\sin i$ for the sample containing unresolved binaries and the equivalent distribution for single stars (dotted line). (c) The distribution of model radii R_m^s determined from the system luminosity relative to the radius of single stars, R_m^a with similar luminosity. (d) The combined effect of the changes in measured $v\sin i$ and predicted R_m on the probability density function of $r\sin i$ for a population containing unresolved binary systems compared with the equivalent distribution for a population of single stars (dotted line).